A homogenisation-based continuum damage mechanics model for cyclic damage in 3D composites

S. Ghosh **J. R. Jain**
ghosh.5@osu.edu **jain.94@osu.edu**
Computational Mechanics Research Laboratory,
Department of Mechanical Engineering,
Ohio State University
Ohio, USA.

ABSTRACT

This paper develops a 3D homogenisation based continuum damage mechanics (HCDM) model for fibre-reinforced composites undergoing micromechanical damage under cyclic loading. Micromechanical damage in a representative volume element (RVE) of the material occurs by fibre-matrix interfacial debonding, which is incorporated in the model through a hysteretic bilinear cohesive zone model. The proposed model expresses a damage evolution surface in the strain space in the principal damage co-ordinate system or PDCS. PDCS enables the model to account for the effect of non-proportional load history. The material constitutive law involves a fourth order orthotropic tensor with stiffness characterised as a macroscopic internal variable. Cyclic damage parameters are introduced in the monotonic HCDM model[1] to describe the material degradation due to fatigue. Three dimensional damage in composites is accounted for through functional forms of the fourth order damage tensor in terms of components of macroscopic strain and elastic stiffness tensor. The HCDM model parameters are calibrated from homogenisation of micromechanical solutions of the RVE for a few representative cyclic strain histories. The proposed model is validated by comparing results of the HCDM model with pure micromechanical analysis results followed by homogenisation. Finally, the potential of cyclic HCDM model as a design tool is demonstrated through macro-micro analysis of cyclic damage progression in composite structures.

NOMENCLATURE

A	resisting area in actual configuration
$\tilde{A}$	effective resisting area in fictitious undamaged configration
$\mathbf{D}$	zero-th, second or fourth order damage tensor
e_{ij}	macroscopic strain tensor
E_{ijkl}	macroscopic elastic stiffness tensor in damaged state
E^0_{ijkl}	macroscopic elastic stiffness tensor in undamaged state
M_{ijkl}	damage effect tensor
P_{ijkl}	damage surface parameters
Q_{ij}	rotation tensor for global co-ordinate system to PDCS
T	cohesive traction vector at the fibre matrix interface
W_d	energy dissipated due to evolving damage
δ	displacement jump at fibre matrix interface
δ_e	critical separation for the cohesive zone
δ_f	cyclic damage parameter for hysteretic cohesive zone
δ_{ij}	Kronekar delta
ε_{ij}	microscopic stress tensor
κ	damage state variable
σ_{max}	maximum traction for the cohesive zone
σ_{ij}	microscopic stress tensor
Σ_{ij}	macroscopic stress tensor
$\tilde{\Sigma}_{ij}$	macroscopic stress tensor in fictitious undamaged configuration

Paper No. 3380. Manuscript received 1 December 2008, revised 26 February 2009, accepted 1 April 2009.

https://doi.org/10.1017/S0001924000003043 Published online by Cambridge University Press

1.0 INTRODUCTION

Composite materials are increasingly being used in automobile, aircraft and other high performance applications because of their improved mechanical properties such as high specific stiffness and strength. These structural components are often subjected to complicated cyclic loading history. Although composites in general have better fatigue life than metals, deficiencies in current life prediction techniques hinder optimal design of composite structures under cyclic loading. Unlike most metals, fatigue damage in composites starts early and grows steadily with deterioration of stiffness in damaged regions causing redistribution of stresses. As a result, prediction of final failure requires complete simulation of cyclic damage progression in the structure. Conventional fatigue life approaches characterise the fatigue damage by macroscopic quantities such as stress/strain and experimentally obtained fatigue life or fatigue strength. Popular approaches for fatigue in metals include stress-life for high cycle fatigue (HCF), strain-life for low cycle fatigue (LCF) and several other models based on S-N or Goodman type diagrams[2].. These concepts have been extended to composites[3,4] and others[5]. These total life approaches, however, do not take into account the actual damage mechanisms such as localised cyclic plastic strains in metals or matrix/interfacial cracks in composites, rendering them empirical in nature.

Experimental investigations have shown reduction in the elastic stiffness during fatigue damage progression in fibre-reinforced composites[6,7]. Phenomenological models have been proposed in the literature characterising fatigue damage through stiffness degradation[8,9]. In this regard, continuum damage mechanics (CDM) models provide a constitutive framework for reflecting damage induced stiffness reduction with the introduction of effective damage parameters that represent overall material degradation[10-12]. Damage and failure of composite materials are inherently multiple scale phenomena coupling different scales of damage initiation and progression. Two types of CDM models, *viz* phenomenological and micromechanical models, have been proposed in the literature for modelling failure of composite materials. The phenomenological CDM models[13-19] employ scalar, second order and fourth order damage tensors using mathematically and thermodynamically consistent formulations of damage mechanics. Damage parameters are identified through macroscopic experiments and in general, they do not explicitly account for damage mechanisms in the microstructure. In 19, a generalised damage law has been developed in terms of cumulative measure of internal sliding for monotonic, hysteretic, dynamic and cyclic loading without explicit consideration of micromechanics. Micromechanics based approaches[20-27], on the other hand conduct micromechanical analysis of a representative volume element (RVE) with subsequent homogenisation, to predict evolving material damage behaviour. The CDM model[25] employs kinematic hardening type damage surface in stress space to account for cyclic damage. The damage surface concept is dropped and loading/unloading during fatigue is determined based on equivalent strain[26]. An arc-tangent form of evolution law for scalar damage evolution is assumed in this case. With the exception of a few[11,20,28,29], most damage models do not account for the evolution of damage or the effect of loading history. Significant error can consequently accrue in the solution of problems, especially those that involve non-proportional loading. Some of these homogenisation studies have overcome this shortcoming through the introduction of simultaneous RVE-based microscopic and macroscopic analysis in each load step[20,30]. However, such approaches can be computationally expensive, especially during fatigue, since detailed micromechanical analyses need to be conducted in each load step at every integration point in elements of the macroscopic structure.

To overcome the shortcomings of macro-micro modelling of composites for predicting damage, Ghosh and coworkers[29,31] have developed a computationally efficient, anisotropic homogenisation based continuum damage mechanics (HCDM) model for composites undergoing microstructural damage. Specifically fibre-matrix interface debonding has been taken as the microstructural damage mechanism in these two dimensional analyses, for which micromechanical analyses are conducted by the Voronoi cell FEM model[32]. This model is constructed by homogenising evolving damage variables in micromechanical analyses of a representative microstructural volume element of the composite. The homogenisation based continuum damage model (HCDM) has been successfully used for macroscopic analysis in multi-scale modelling of composites undergoing fibre-matrix interfacial debonding[31]. In a multi-scale modelling framework, the use of a continuum damage mechanics model in regions of non-critical diffused damage evolution makes the overall computing extremely efficient. This model can avoid the need to perform micromechanical analysis at each load increment. However, it is necessary to zoom into the microstructure and perform pure microscopic analysis in critical regions of dominant crack propagation or localised instability to accurately predict catastrophic failure[31].

The 2D HCDM model[29] does not incorporate the effects of the path dependent load history on the parameters in the damage model. Hence its predictions are not accurate for e.g. non-proportional loading cases. The authors have developed a 3D HCDM model[1,33] that overcomes these limitations through the introduction of a principal damage coordinate system (PDCS), which evolves with the load history. The objective of the present work is to develop a unified continuum damage modelling framework that employs same damage evolution law for monotonic as well as fatigue damage. To account for fatigue damage, cyclic damage parameters are introduced in the monotonic damage surface. The 3D HCDM model introduces functional forms of a fourth order damage tensor in terms of macroscopic strain and stiffness tensor components that are calibrated by micromechanical RVE analysis along different strain loading paths. Anisotropy and its evolution are also effectively treated in this model. Parametric representation of various damage tensors significantly enhances the computational efficiency by avoiding cumbersome strain space interpolations[29]. The HCDM model can be conveniently incorporated in any finite element code, e.g. ABAQUS or MARC for efficient modelling of damage evolution in composite structures due to degrading microstructures.

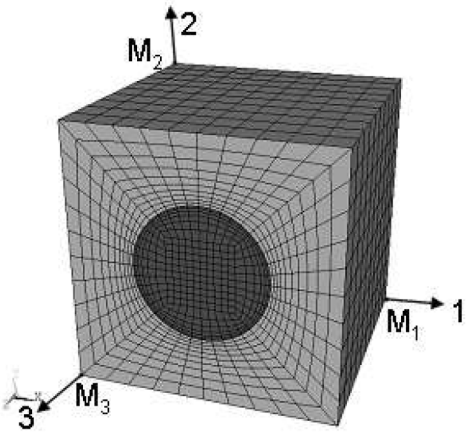
The CDM model proposed has two main attributes. It has a very strong connection with the micromechanical phenomena. For example, one can relate the macroscopic damage energy to the amount of debonding or fibre cracking in the microstructure for any composite architecture. Thus, it can be used as an effective tool for microstructure design. The second is that the CDM model overcomes the necessity for tedious micro-macro computations, while getting similar accuracy and dependence on the microstructure and micromechanics. Hence it can be coupled and used in any commercial software for macro-scale structural analyses.

This paper starts with a brief overview of continuum damage mechanics and establishes significance of PDCS in Section 2. Section 3 describes the micromechanical model with interfacial debonding followed by its homogenisation. After conducting studies in 1D, Section 4 develops a homogenisation based orthotropic CDM or HCDM model in the PDCS. This section also discusses parameter calibration for monotonic and cyclic loading. Section 5 provides the stress update procedure with HCDM in its implementation in a macroscopic finite element code for structural analysis. Validation of the HCDM model for a single fibre RVE subjected to cyclic loading is presented in Section 6. This section also presents demonstrative structural application to show the capabilities of the HCDM model. The paper concludes with a brief summary of the developed model.

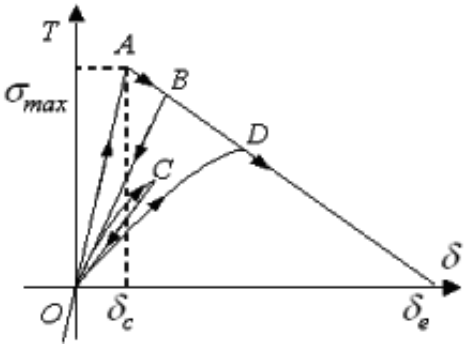
2.0 ANISOTROPIC CONTINUUM DAMAGE MECHANICS

The general form of CDM models[10], introduces a fictitious stress $\tilde{\Sigma}_{ij}$ acting on an effective resisting area ($\tilde{A}$). This is caused by reduction of the original resisting area A due to material degradation due to the presence of micro-cracks and stress concentration in the

https://doi.org/10.1017/S0001924000003043 Published online by Cambridge University Press



(a)



(b)

Figure 1. (a) Finite element mesh and (b) hysteretic cohesive zone model at the fibre-matrix interface for the RVE with a cylindrical fibre.

vicinity of cracks. In Refs 14 and 29, the effective stress $\tilde{\Sigma}_{ij}$ is related to the actual Cauchy stress Σ_{ij} through a fourth order damage effect tensor M_{ijkl} as

$$\tilde{\Sigma}_{ij} = M_{ijkl}(D)\Sigma_{kl} \quad \ldots (1)$$

where M_{ijkl} is a function of a damage tensor $\mathbf{D}(= D_{ijkl}\,\mathbf{e_i}\otimes\mathbf{e_j}\otimes\mathbf{e_k}\otimes\mathbf{e_l})$. $\mathbf{D}$ can be a zeroth, second or fourth order tensor, depending on the model employed. As discussed in Refs 11 and 34, the hypothesis of equivalent elastic energy is used to evaluate M_{ijkl} and establish a relation between the damaged and undamaged stiffnesses as

$$W_C(\Sigma,\mathbf{D}) = \frac{1}{2}(E_{ijkl}(\mathbf{D}))^{-1}\Sigma_{ij}\Sigma_{kl} = W_C(\tilde{\Sigma},\mathbf{0}) = \frac{1}{2}(E^o_{ijkl})^{-1}\tilde{\Sigma}_{ij}\tilde{\Sigma}_{kl} \quad \ldots (2)$$

where $\Sigma = \Sigma_{ij}\mathbf{e_i}\otimes\mathbf{e_j}$, E^o_{ijkl} is the elastic stiffness tensor in the undamaged state and $E_{ijkl}(\mathbf{D})$ is the stiffness in a damaged state. From Equations (1) and (2), the relation between the damaged and undamaged stiffnesses is established as

$$E_{ijkl} = (M_{pqij})^{-1}E^o_{pqrs}(M_{rskl})^{-T} \quad \ldots (3)$$

where the exponent $-T$ corresponds to the transpose of the inverse of the fourth order $\mathbf{M}$ tensor. With the choice of an appropriate order of the damage tensor and the assumption of a function for M_{ijkl}, Equation (3) can be used to formulate a damage evolution model using micromechanics and homogenisation.

2.1 Principal damage co-ordinate system (PDCS)

For a second order damage tensor D_{ij}, the damage effect tensor M_{ijkl} in Equation (1) has been formulated[35] as:

$$M_{ijkl} = (\delta_{ik} - D_{ik})^{-1}\delta_{jl} \quad \ldots (4)$$

D_{ij} is symmetric and it can describe the damage states which have at least orthotropic symmetry. For any arbitrary D_{ij} the corresponding effective stress tensor, obtained by substituting Equation (4) in Equation (1), may be unsymmetric. An implicit method of rendering the stress tensor symmetric has been suggested[11], which is used to derive the inverse of the damage effect tensor $[\mathbf{M}(D_{ij})]^{-1}$. The present work assumes orthotropy of the homogenised stiffness matrix in the principal damage co-ordinate system. For known values of E^0_{ijkl} and E_{ijkl}, Equation (3) results in a system of nonlinear algebraic equations in D_{ij}, which are solved by nonlinear least squares minimisation. Subsequently, the eigen-vectors of D_{ij}, *viz* $\mathbf{e_{D1}}$, $\mathbf{e_{D2}}$ and $\mathbf{e_{D3}}$ are evaluated and the transformation matrix $[\mathbf{Q}]^D = [\mathbf{e_{D1}}\ \mathbf{e_{D2}}\ \mathbf{e_{D3}}]^T$ is formed. The rotation matrix $[\mathbf{Q}]^D$ transforms the global co-ordinate system to the principal damage co-ordinate system.

2.2 Evolution of PDCS for different load histories

Evolution of PDCS with different load histories is examined in Ref. 1 by conducting micromechanical analysis of RVE with a single fibre of 20% volume fraction shown in Fig. 1(a). To allow debonding, the fibre-matrix interface is modelled using cohesive zone elements as discussed in Section 3. Micromechanical analysis is followed by homogenisation to evaluate evolving stiffnesses and PDCS in the composite. Two combined loading histories are considered for the analyses: Case (a): proportional loading, and Case (b): non-proportional loading. The final state of the macroscopic strain e_{ij} is identical for both the cases. For the proportional loading case (a), the orientation of the damage axes jumps to 24° and remains unchanged at this value with respect to the global axes throughout damaging process. For the non-proportional loading case (b), the PDCS continuously rotates to a final position of 21° orientation. Certainly in this case, the PDCS rotation should be incorporated in the HCDM model to account for the damage history.

3.0 MICROMECHANICAL RVE MODEL AND HOMOGENISATION

3.1 Cohesive zone model for interfacial debonding

A 3D micromechanical model for composite microstructures undergoing fibre-matrix interfacial debonding has been developed[36] based on bilinear cohesive law. The model has been extended[37] to include irreversible hysteretic effects in mixed-mode failures. In this work, the hysteretic bilinear cohesive zone model is employed to simulate fibre-matrix interfacial debonding with fatigue damage accumulation.

In the bilinear cohesive zone element of Ref. 36, the relation between traction $T(=\sqrt{T_n^2 + T_{t1}^2 + T_{t2}^2})$ and the effective opening displacement $\delta(=\sqrt{\delta_n^2 + \beta^2\delta_t^2})$ is given as

https://doi.org/10.1017/S0001924000003043 Published online by Cambridge University Press

$$T = \begin{cases} \dfrac{\sigma_{max}}{\delta_c}\delta & \text{if}(\delta \le \delta_c) \quad \text{(hardening region)} \\ \dfrac{\sigma_{max}}{\delta_c - \delta_e}(\delta - \delta_e) & \text{if}(\delta_c < \delta \le \delta_e) \quad \text{(softening region)} \\ 0 & \text{if } (\delta \ge \delta_e) \quad \text{(complete debonding)} \end{cases} \quad \ldots (5)$$

where (T_n, T_{t1}, T_{t2}) are normal and tangential components of the inter facial traction, (δ_n, $\delta_t = \sqrt{\delta_{t_1}^2 + \delta_{t_2}^2}$) are displacement jumps in normal and tangential directions respectively and β is an empirical factor.

For a positive normal displacement δ_n, the traction at the interface increases linearly to a maximum value of corresponding to δ_c. After that, the traction starts decreasing with increasing separation and finally reaches zero at a value of δ_e. The unloading behaviour in the hardening region follows the same slope as that of the loading path. In the softening region, unloading is assumed to follow a linear path back from the current position to the origin with a reduced stiffness. Reloading follows the unloading slope till it meets the point of unloading in the softening plot, and then continues along the softening plot. When the normal displacement is negative, stiff penalty springs are introduced to prevent penetration. Details of the implementation of 3D cohesive zone elements in the user defined element (UEL) subroutine of FE code ABAQUS has been discussed in Ref. 36.

To account for dissipative mechanisms in the fracture process zone ahead of the crack tip in cyclic loading, the hysteretic model incurs fatigue damage during reloading. Unloading is still assumed to be linearly elastic towards the origin of traction-separation curve. During reloading the cohesive spring stiffnesses in normal and tangential directions are assumed to decay according to the stiffness degradation law given by:

$$\dot{K} = \begin{cases} -K\dfrac{\dot{\delta}}{\delta_f} & \text{if } \dot{\delta} > 0 \\ \text{if } \dot{\delta} \le 0 \end{cases} \quad \ldots (6)$$

where the material parameter δ_f governs the rate of stiffness decay during cyclic loading. The hysteretic response of the cohesive model remains within the envelope of the bilinear model. When the reloading curve intersects the softening curve, it follows the curve and accrues only monotonic damage as illustrated in Fig. 1(b). Further details of numerical implementation of the hysteretic cohesive zone element are discussed in Ref. 37.

3.2 Homogenisation and stiffness evaluation

Components of the homogenised elastic stiffness tensor E_{ijkl}, are calculated by solving six independent micromechanical boundary value problems of the RVE. The RVE in each case is subjected to periodicity displacement conditions on the boundary. For a given macroscopic or average strain e_{ij}, the corresponding nodes of opposite faces (say n_2^p and n_1^p) of the RVE are constrained as[38].

$$(u_i)_{n_2^p} - (u_i)_{n_1^p} = e_{ij}\Delta x_j \quad \ldots (7)$$

where Δx_i are the relative co-ordinates of nodes on opposite faces. Macroscopic strains are then applied by fixing a corner node and specifying the displacement on master nodes M_1, M_2 and M_3 that belong to orthogonal faces as shown in Fig. 1(a). Elastic stiffness E_{ijkl} is evaluated by applying single unit strain components to the RVE. These correspond to six boundary value problems, for example, e_{11}, all other components = 0 etc. Finally, the homogenised or macroscopic stresses Σ_{ij} and strains e_{ij} are obtained by volume averaging.

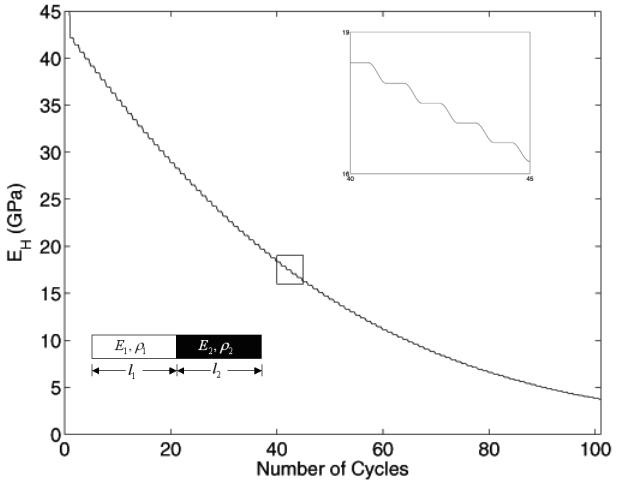


Figure 2. Gradual decrease of the homogenised elastic modulus E_H of the layered composite RVE subjected to cyclic loading.

4.0 EVOLUTION EQUATIONS FOR THE HCDM MODEL

4.1 One-dimensional HCDM model for layered composites

In order to understand the phenomenon of damage evolution in composites under cyclic loading, a one-dimensional (1D) problem of layered composite media is considered. The microstructural RVE, shown in inset of Fig. 2, is modelled as two continuum bar elements with a hysteretic cohesive zone sandwiched between them. This represents a weak interface between adjacent layers. The elastic modulii of the layers are E_1 = 717GPa and E_2 = 123GPa, and the cohesive zone parameters for the interface are $\delta_c = 5{\cdot}0 \times 10^{-5}$m, $\delta_e = 20 \times 10^{-4}$m, $\delta_f = 20 \times 10^{-3}$m and σ_m = 0·02GPa. With an applied macroscopic strain e, this results in a nonlinear boundary value problem that can be solved analytically using a linearised rate form. The resulting expression for the homogenised response is given as

$$\dot{\Sigma} = \frac{(l_1 + l_2)k_t E_1 E_2}{(l_1 E_2 + l_2 E_1)k_t + E_1 E_2}\dot{e} \quad \ldots (8)$$

where k_t is the tangent stiffness of the hysteretic traction-separation law in Equations (5) and (6) and l_1 and l_2 are lengths of the layers. The homogenised elastic modulus E_H can be calculated by evaluating the incremental solution in Equation (8).

An anisotropic CDM model in strain-space involving fourth order orthotropic damage tensor has been proposed in Ref. 1 for damage in composites under monotonic loading. For the one dimensional problem, the damage evolution surface of Ref. 1 takes the following form:

$$F = \frac{1}{2}ePe - \kappa(W_d) = 0 \quad \ldots (9)$$

where P is damage surface parameter, $\kappa(W_d)$ is damage state variable, and W_d is the dissipation of the strain energy density due to stiffness degradation, expressed as:

$$W_d = \int \frac{1}{2} ee\, dE \quad \ldots (10)$$

The rate of stiffness degradation is given as

https://doi.org/10.1017/S0001924000003043 Published online by Cambridge University Press

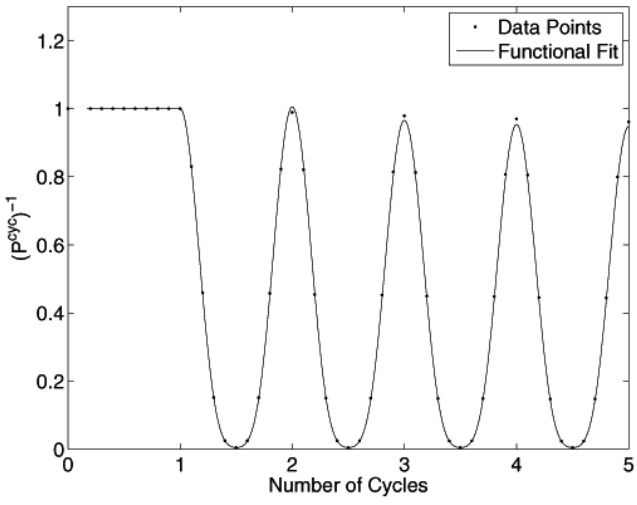


Figure 3. Functional representation of P^{cyc} for the one-dimensional problem.

$$\dot{E} = \dot{\lambda}\frac{\partial F}{\partial(\frac{1}{2}e^2)} = \dot{\lambda}P \qquad \ldots (11)$$

As there is only one possible monotonic strain path in 1D, P =1 during monotonic damage. To develop a continuum damage model for cyclic loading, numerical studies are performed in 1D for fatigue damage evolution in the layered media. Figure 2 shows degradation of homogenised elastic modulus E_H under cyclic loading that is obtained using analytical solution in Equation (8). As the problem is one-dimensional, the microscopic loading/unloading are directly related to their macroscopic counterparts. The modulus E_H decreases rapidly from an initial value of 180GPa till when the applied macro-strain reaches a maximum value during the first cycle. This corresponds to monotonic damage in the cohesive zone of RVE (line $O - A - B$ in Fig. 1(b)). As the strain reduces to a minimum value, the modulus remains constant, corresponding to unloading in the cohesive zone (line $B - O$ in Fig. 1(b)). The modulus starts decreasing steadily during the reloading, corresponding to fatigue damage in the cohesive zone (line $O - C$ in Fig. 1(b)). Beyond the first cycle, the modulus degrades steadily during reloading within each cycle due to fatigue damage.

To describe such behaviour, a cyclic damage surface parameter P^{cyc} is introduced in the monotonic HCDM model. The variation of P^{cyc} is studied by explicitly calculating its values from 1D analytical results. Enforcing consistency condition $F_{n+1} = 0$ for $n - th$ load increment, the scalar multiplier λ_{n+1} is determined using backward Euler method as

$$\lambda_{n+1} = \lambda_n + \frac{\frac{1}{2}e_{n+1}((E_H)_{n+1} - (E_H)_n)e_{n+1}}{\kappa_{n+1}} \qquad \ldots (12)$$

Subsequently, P^{cyc} is calculated as

$$P^{cyc}_{n+1} = \frac{(E_H)_{n+1} - (E_H)_n}{\lambda_{n+1} - \lambda_n} \qquad \ldots (13)$$

With evolving damage during reloading, the strain state should remain on the damage surface throughout the unloading. This is accomplished by varying P^{cyc} during unloading. Figure 3 shows the data points for P^{cyc} obtained for a reference cyclic loading path. The following parametric function is obtained for P^{cyc} by least squares minimisation:

$$P^{cyc} = d_0 + \frac{Ee}{d_1 E + d_2} + \frac{d_3}{e^2} \qquad \ldots (14)$$

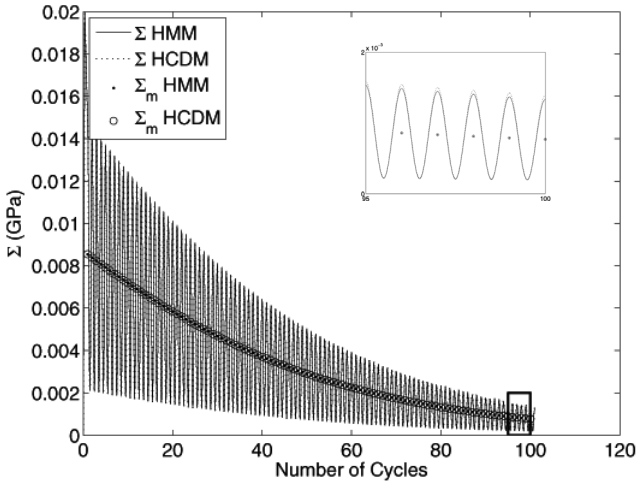


Figure 4. Comparison of macroscopic stress obtained using 1D HCDM model and homogenised micromechanics (HMM) for layered composite under cyclic loading.

Once the parametric representation of P^{cyc} is determined, a stronger condition for satisfying consistency may be used by setting $\dot{F}(e, E, W_d) = 0$. The scalar multiplier λ in this case is given as

$$\dot{\lambda} = \frac{P\dot{e} + \frac{1}{2}e\frac{\partial P}{\partial e}\dot{e}}{\left(\frac{\partial \kappa}{\partial W_d} - \frac{\partial P}{\partial E}\right)\frac{1}{2}eP} \qquad \ldots (15)$$

The procedure for conducting macroscopic analysis using the calibrated HCDM model is discussed in Section 5 for 3D composites. Numerical validation of the 1D model is presented here. The macroscopic stress plot in Fig. 4 compares the 1D HCDM model predictions with the homogenised micromechanics (HMM) results for applied cyclic loading of $e = e_m + e_a\text{Sin}(\omega t)$ with mean strain $e_m = 2e - 4$, amplitude $e_a = 1{\cdot}5e - 4$, and $\omega = 2\pi$. Excellent agreement between HMM and HCDM results is seen for the 100 cycles simulated. The mean stress Σ_m shown by points (HMM) and circles (HCDM) in Fig. 4 show similar agreement. Based on inferences drawn from the 1D model, a 3D HCDM model for cyclic loading is developed in the following sections.

4.2 Orthotropic HCDM model for 3D composites

The anisotropic CDM model involving fourth order damage tensor, proposed in Ref. 29, introduces a damage evolution surface to delineate the interface between damaged and undamaged domains in the strain-space (e_{ij}). In this work, a damage evolution surface that is valid for monotonic as well as cyclic loading is proposed. To account for non-proportional loading history, the evolution equations are written in the principal damage co-ordinate system (PDCS) as

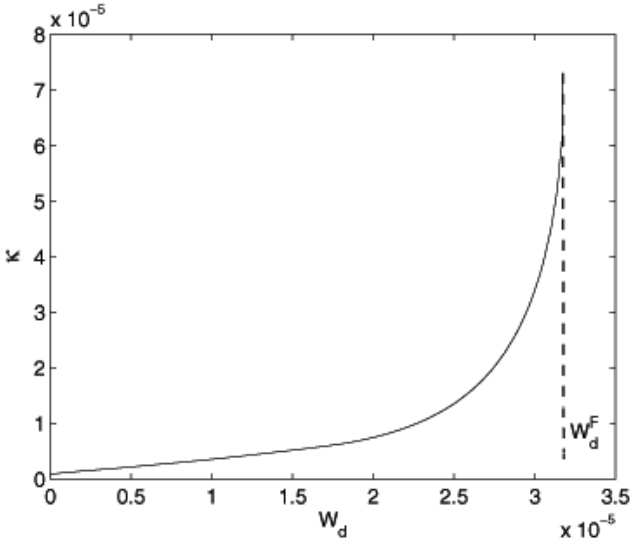
$$F' = \frac{1}{2}e_{ij}'(P^{mon}P^{cyc})'_{ijkl}e_{kl}' - \kappa'(\alpha W_d') \qquad \ldots (16)$$

where *mon* and *cyc* in the superscript denote monotonic and cyclic loading respectively. W_d' is the dissipation of the strain energy density due to stiffness degradation and is expressed as:

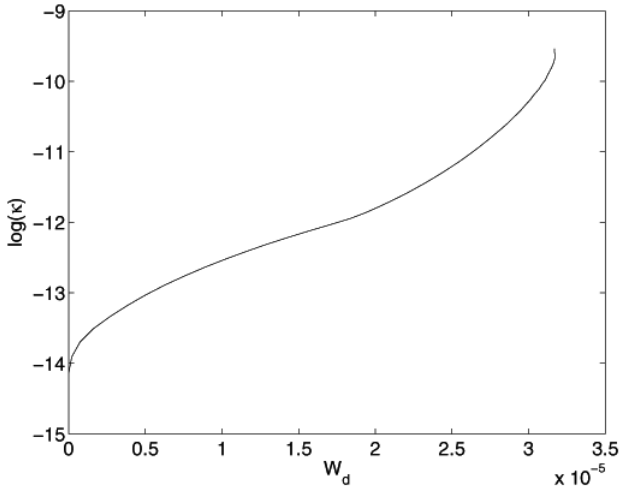
$$W_d' = \int\frac{1}{2}e_{ij}'e_{kl}'\mathrm{d}E'_{ijkl} \qquad \ldots (17)$$

where the prime in the superscript denotes quantities expressed in the PDCS using the transformation laws

https://doi.org/10.1017/S0001924000003043 Published online by Cambridge University Press



(a)



(b)

Figure 5. (a) $\kappa - W_d$ and (b) $\log(\kappa) - W_d$ plots for a 3D RVE with circular fibre subjected to uniaxial tension.

$$E_{ijkl}' = Q_{ip}Q_{jq}Q_{kr}Q_{ls}E_{pqrs} \quad \text{and} \quad e_{ij}' = Q_{ik}Q_{jl}e_{kl} \qquad \ldots (18)$$

and Q_{ij} is the transformation matrix. $P'_{ijkl} = (P^{mon}P^{cyc})'_{ijkl}$ is a fourth order symmetric negative definite tensor that corresponds to the direction of the rate of stiffness degradation tensor E'_{ijkl}. The fourth order tensor P'^{mon}_{ijkl} describes damage due to monotonic loading and remains constant during cyclic loading. The fourth order tensor P'^{cyc}_{ijkl} is introduced to account for damage due to cyclic loading. When inactive, components P'^{cyc}_{ijkl} assume unit values, recovering the monotonic HCDM model. $\kappa'(W\alpha'_d)$ is a damage state variable and is a scaling parameter.

Damage evolution takes place when $F' > 0$. In this case, consistency condition $F' = 0$ is satisfied and, assuming associativity rule in the stiffness space, the rate of stiffness degradation in PDCS is given as

$$\dot{E}_{ijkl}' = \dot{\lambda}\frac{\partial F'}{\partial(\frac{1}{2}e_{ij}'e_{kl}')} = \dot{\lambda}(P^{mon}P^{cyc})'_{ijkl} \qquad \ldots (19)$$

Section 4.3 introduces functional representations for various HCDM model parameters and Section 4.4 details the procedure for determination of these parameters from micromechanics and homogenisation.

4.3 Parametric forms in 3D HCDM model

4.3.1. Damage state variable κ'

The damage function $\kappa'(W'_d)$ is evaluated for a reference monotonic loading path, and results for all other strain paths are scaled with respect to this reference value. For the reference monotonic loading path ($e'_{11} \neq 0$, all other $e'_{ij} = 0$), setting $P'_{1111} = 1$, is determined from damage surface of Equation (16) as

$$\kappa' = \frac{1}{2}(e'_{11})^2 \qquad \ldots (20)$$

The function $\kappa'(W_d)$ is determined from the micromechanical analysis by evaluating W_d at each strain increment. The $\kappa' - W_d$ plot for uniaxial tension case is shown in Fig. 5(a). W_d remains zero till κ' exceeds a threshold value corresponding to the initiation of debonding induced microscopic damage. Subsequently, W_d increases rapidly, signaling substantial material deterioration during the initial stages of damage. Eventually, W_d saturates at a value W_d^F corresponding to configuration with arrested debond or fully debonded interface. Very little material degradation due to damage occurs beyond this saturation value. The behaviour of the plot is similar for different strain histories with the exception that the value of W_d^F differs. The variability of W_d^F with different loading paths is taken into account[1] by developing functional forms of κ', explicitly describing its dependence on the macroscopic strain components e_{ij} and W_d. Three invariant forms of the strain components, consistent with anisotropic material properties, are used in these functions. They are:

$$\begin{aligned} I_1 &= \frac{1}{3}\left(Ae_{11} + Be_{22} + Ce_{33}\right) \\ J_2 &= F\left(e^d_{22} - e^d_{33}\right)^2 + G\left(e^d_{33} - e^d_{11}\right)^2 \\ &+H\left(e^d_{11} - e^d_{22}\right)^2 + L\left(e^d_{12}\right)^2 + M\left(e^d_{13}\right)^2 + N\left(e^d_{23}\right)^2 \\ J_3 &= O\left(e^d_{11}e^d_{22}e^d_{33}\right) + P\left(e^d_{11}(e^d_{23})^2\right) \\ &+Q\left((e^d_{12})^2 e^d_{33}\right) + R\left(e^d_{13}e^d_{12}e^d_{23}\right) + S\left((e^d_{13})^2 e^d_{22}\right) \end{aligned} \qquad \ldots (21)$$

where $e^d_{ij} = e_{ij} - \frac{1}{3}\delta_{ij}e_{kk}$ is the deviatoric strain tensor. The invariant forms I_1, J_2 and J_3 are respectively linear, quadratic and cubic functions of e_{ij}. A, B, C, ..., S are introduced to characterise the state of anisotropy in the damaged material. Numerical investigations show that A, B, C, ..., S depend on energy dissipated due to damage W_d and are assumed to be quadratic functions of W_d given as

$$\begin{aligned} A(W_d) &= a_0^A + a_1^A W_d + a_2^A W_d^2, \\ B(W_d) &= a_0^B + a_1^B W_d + a_2^B W_d^2, \qquad C(W_d) = \ldots \end{aligned} \qquad \ldots (22)$$

A parametric representation involving tangent function is proposed for κ' in Ref 1. Figure 5(b) shows plot of $\log(\kappa')$ as a function of W_d. It can been seen that the $\kappa' - W_d$ relation is simplified in the logarithmic space to a polynomial function. Therefore, functional form for κ' is proposed as:

$$\begin{aligned} &\log(\kappa' - \kappa'_0) = f(I_1, J_2, J_3) = a_0 + a_1 I_1 + a_2 J_2 \\ &+a_3 J_3 + a_4 I_1^2 + a_5 I_1 J_2 + \ldots \end{aligned} \qquad \ldots (23)$$

https://doi.org/10.1017/S0001924000003043 Published online by Cambridge University Press

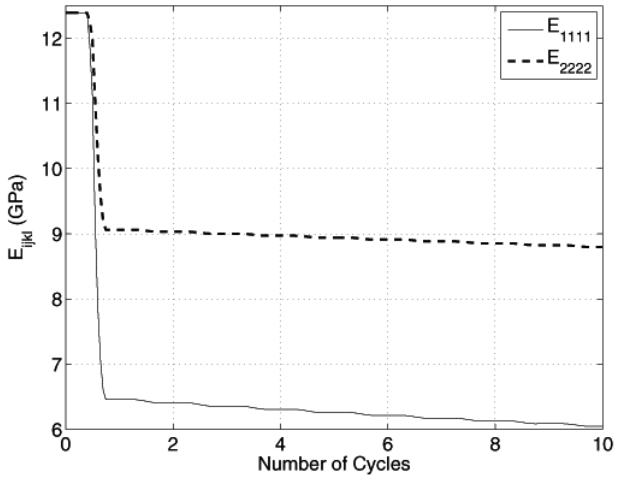


Figure 6. Degradation of components of elastic stiffness for the 3D RVE tensor due to cyclic loading.

4.3.2. Damage surface parameter P'^{mon}_{ijkz} for monotonic loading

The direction of the rate of stiffness degradation varies continuously with damage evolution with increasing loads. From Equation (19) this implies that P'^{mon}_{ijkl} also varies accordingly. Based on previous work reported in Ref. 1 and parametric studies from micromechanics, a polynomial function form is assumed for the components P'^{mon}_{ijkl} in terms of the anisotropic invariant forms of strain defined in Equation (21) as

$$P'^{mon}_{ijkl}(I_1,J_2,J_3) = f^{ijkl}(I_1,J_2,J_3) = c_0^{ijkl} + c_1^{ijkl}I_1 + c_2^{ijkl}J_2 + c_3^{ijkl}J_3 + c_4^{ijkl}I_1^2 + c_5^{ijkl}I_1J_2 + \ldots \quad \ldots (24)$$

4.3.3. Damage surface parameter P'^{cyc}_{ijkz} for cyclic loading

To develop parametric representation of damage surface parameters P'^{cyc}_{ijkl}, parametric studies are conducted by performing micromechanical simulations of the single fibre RVE subjected to cyclic loading. Figure 6 shows evolution of components of elastic stiffness tensor E'_{ijkl} under cyclic loading. The stiffness degrades rapidly during the first cycle owing to monotonic damage. After the first cycle, stiffness degrades steadily due to fatigue damage. Within a cycle, the stiffness degrades during loading, remains constant during unloading, and again degrades during reloading. This indicates that the damage surface parameters have inverse relation with strain such that the strain state remains on the damage surface during unloading. Parametric studies also show that the rate of elastic stiffness degradation depends on current elastic stiffness. This behaviour is consistent with the hysteretic cohesive law in Equation (6). In addition, the parametric function should have well defined derivatives with respect to its arguments. Considering these requirements, a parametric functional form involving components of secant stiffness tensor E'_{ijkl} and the Frobenius norm $||\,e'\,||$ of strain tensor is proposed for . The parametric form is given as

$$P'^{cyc}_{ijkl} = d_0^{ijkl} + \frac{E_{ijkl}'\,||\,e'\,||}{d_1^{ijkl}E_{ijkl}' + d_2^{ijkl}} + \frac{d_3^{ijkl}}{||\,e'\,||^2} \quad \text{(nosum)} \quad \ldots (25)$$

where the Frobenius norm of the strain tensor $||\,e'\,||$ is given as

$$||\,e'\,|| = \left(e'_{ij}e'_{ij}\right)^{\frac{1}{2}} \quad \ldots 26)$$

4.4 Parameter calibration for 3D HCDM model

The procedure for calibrating HCDM model parameters from micromechanics and homogenisation is discussed in Ref. 1. This procedure is based on determination of scalar multiplier $\dot{\lambda}$ by satisfaction of the consistency condition at discrete increments. Denoting the beginning and end of the n-th increment by subscripts n and $n+1$ respectively, the consistency condition is written as $F'_{n+1} = 0$. Although such approach for consistency condition is generally used and yields acceptable results, a more accurate approach is presented in this work. The expression for $\dot{\lambda}$ is obtained by analytically satisfying the consistency condition $\dot{F}' = 0$. Assuming parametric representations of κ', P'^{mon}_{ijkl} and P'^{cyc}_{ijkl} given in Equations (23), (24) and (25) respectively, the consistency condition corresponding to damage surface in Equation (16) is written as

$$\dot{F}' = \frac{\partial F'}{\partial e_{ij}'}\dot{e}_{ij}' + \frac{\partial F'}{\partial W_d'}\dot{W}_d' + \frac{\partial F'}{\partial E_{ijkl}'}\dot{E}_{ijkl}' = 0 \quad \ldots (27)$$

or

$$\frac{\partial}{\partial e_{ij}'}\left(\frac{1}{2}e_{pq}'P'_{pqrs}e_{rs}'\right)\dot{e}_{ij}' - \frac{\partial \kappa'}{\partial e_{ij}'}\dot{e}_{ij}' + \frac{\partial P'_{ijkl}}{\partial W_d'}\dot{W}_d'\frac{1}{2}e_{ij}'e_{kl}' - \frac{\partial \kappa'}{\partial W_d'}\dot{W}_d' + \frac{1}{2}e_{ij}'e_{kl}'\frac{\partial P'_{ijkl}}{\partial E_{pqrs}'}\dot{E}_{pqrs}' = 0 \quad \ldots (28)$$

The rate of degradation in Equation (19) and definition of W_d in Equation (17) leads

$$\dot{W}_d = \frac{1}{2}e'_{ij}e'_{kl}\dot{E}'_{ijkl} = \frac{1}{2}e'_{ij}e'_{kl}\dot{\lambda}P'_{ijkl} \quad \ldots (29)$$

The scalar multiplier $\dot{\lambda}$ is then determined as

$$\dot{\lambda} = \frac{e_{pq}'P'_{pqrs}\dot{e}_{rs}' + \frac{1}{2}e_{pq}'e_{rs}'\frac{\partial}{\partial e_{ab}'}(P'_{pqrs})\dot{e}_{ab}' - \frac{\partial \kappa'}{\partial e_{ab}'}\dot{e}_{ab}'}{\left(\frac{\partial \kappa'}{\partial W_d'} - \frac{1}{2}e_{ij}'e_{kl}'\frac{\partial P'_{ijkl}}{\partial W_d'}\right)\frac{1}{2}e_{lm}'P'_{lmno}e_{no}' + \frac{1}{2}e_{ij}'e_{kl}'\frac{\partial P'_{ijkl}}{\partial E_{lmno}'}P'_{lmno}} \quad \ldots (30)$$

The various derivatives required for evaluating $\dot{\lambda}$ using Equation (30) are provided in the Appendix.

To determine the coefficients in the parametric representations for κ', P'^{mon}_{ijkl}, and P'^{cyc}_{ijkl} in Equations (22), (23), (24), and (25), micromechanical analysis of the single fibre RVE is conducted for N_{ref} different strain histories, and the values of $(E'_{ijkl})_{ref}$ and $(W'_d)_{ref}$ are explicitly computed. A sufficient number of reference strain paths are selected such that the parametric functions represent all possible strain history in field simulations. The coefficients are determined such that the consistency condition for damage surface in Equation (16) and the associative degradation rule in Equation (19) are satisfied for each strain state in the reference paths. The procedure is summarised as follows:

4.4.1 Monotonic loading

1. Perform micromechanical analysis along few monotonic reference strain paths. Compute and store values of $(E'_{ijkl})_{ref}$ and $(W'_d)_{ref}$ for N_{ref} different strain histories.
2. At the start of each iteration algorithm, assume starting values for coefficients in Equations (22), (23)) and (24).

- For the I^{th} iteration, evaluate $(P'^{mon}_{ijkl})^I$ using Equation (24) for each strain state e_{ij} in the reference paths considered.
- For each strain state, evaluate $(\lambda)^I_{n+1}$ by integrating Equation (30) with backward Euler method. The cyclic damage parameters P'^{cyc}_{ijkl} are inactive during monotonic loading and assume unit values. The corresponding derivatives vanish in Equation (30).

https://doi.org/10.1017/S0001924000003043 Published online by Cambridge University Press

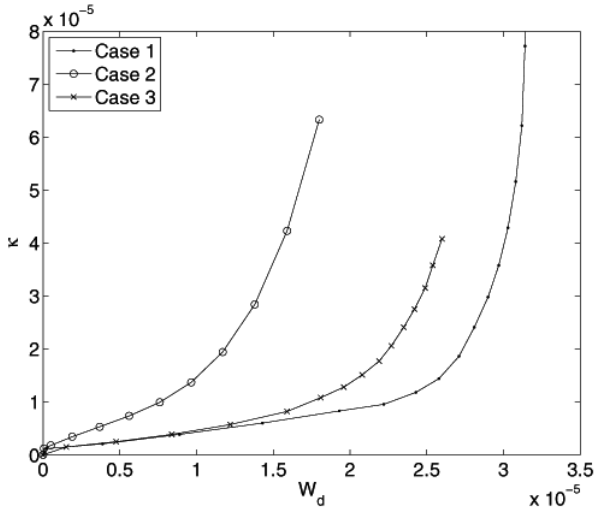
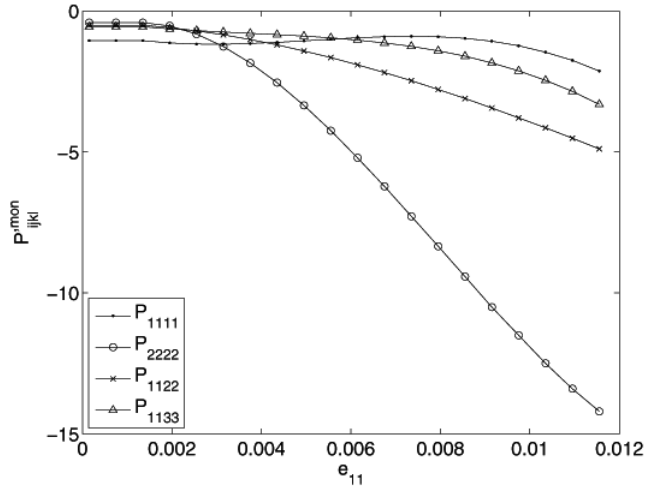
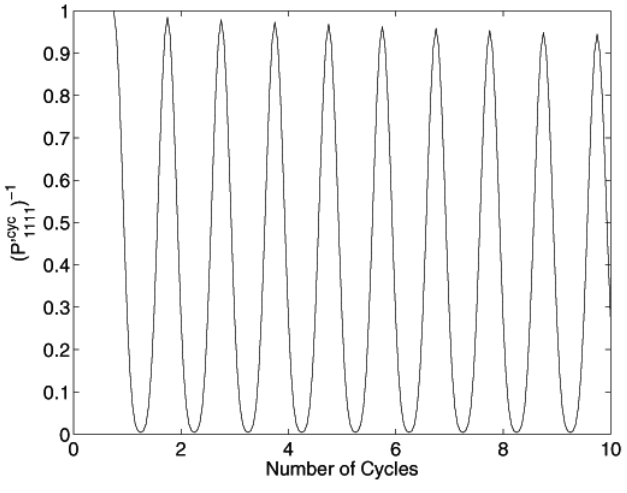


Figure 7. Functional representation of the $\kappa' - w_d$ relation obtained from homogenised micromechanics.



(a)



(b)

Figure 8. Functional representation of (a) P'^{mon}_{ijkl} and (b) P'^{cyc}_{1111} for uniaxial tension from homogenised micromechanics.

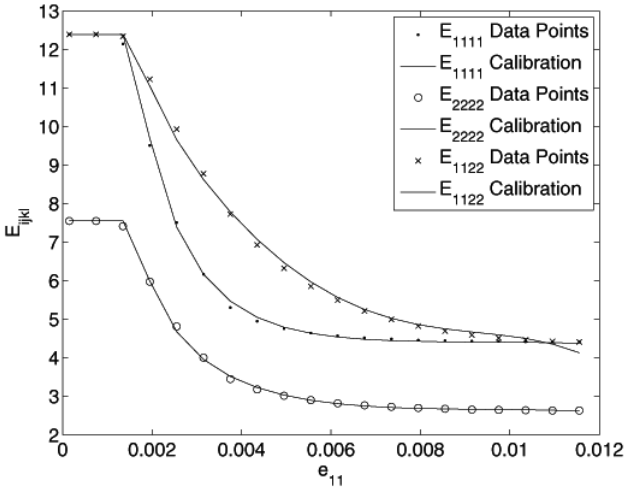


Figure 9. Degradation of components of elastic stiffness tensor during monotonic loading: least squares determination of HCDM model parameters.

- Calculate the least squares residual as

$$RESIDUAL = \sum_{ref=1}^{N_{ref}} \left[\dot{E}'_{ijkl} - \left(\dot{\lambda} P'_{ijkl} \right)^I \right]^2_{ref} \quad \ldots (31)$$

where N_{ref} is the total number of strain states in the reference paths considered.

- Stop if the convergence in the coefficients is achieved, i.e. ($RESIDUAL \leq TOL$). Otherwise make a new guess for the coefficients and continue iteration.

3. Store the values of coefficients obtained using least squares minimisation for subsequent use in macroscopic analysis with the HCDM model.

Figures 7 and 8(a) show the resulting functions for κ' and P'^{mon}_{ijkl} that minimise the least squares residual in Equation (31). Fifth order polynomial functions in Equations (23) and (24) yield good convergence properties for the least square residual. Figure 9 satisfactorily compares the degradation of elastic stiffness obtained using functions in Figs 7 and 8(a) by least squares minimisation, with the homogenised micromechanical results (HMM) for the uniaxial tension case.

4.4.2. Cyclic loading

1. Perform micromechanical analysis along few cyclic reference strain paths. Compute and store values of $(E'_{ijkl})_{ref}$ and $(W'_d)_{ref}$ for N_{ref} different strain histories
2. At the start of each iteration algorithm, assume starting values for coefficients in Equation (25)

- For the I^{th} iteration, evaluate $(P'^{cyc}_{ijkl})^I$ using Equation (25) for each cyclic strain state e_{ij} in the reference paths considered.
- For each damaging strain state, evaluate $(\lambda)^I_{n+1}$ by integrating Equation (30) with backward Euler method. The coefficients in function for κ' in Equation (23) are known from calibration of the monotonic HCDM model. The parameters P'^{mon}_{ijkl} remain constant and the corresponding derivatives vanish in Equation (30). In this case, calculate the least squares residual as

https://doi.org/10.1017/S0001924000003043 Published online by Cambridge University Press

$$RESIDUAL = \sum_{ref=1}^{N^d_{ref}} \left[\dot{E}'_{ijkl} - \left(\dot{\lambda} P'_{ijkl} \right)^I \right]^2_{ref} \quad \ldots (32)$$

where N^d_{ref} is the total number of damaging strain states in the reference paths considered

- For each elastic unloading strain state, $\dot{\lambda} = 0$ as no damage evolution takes place. In this case, $\kappa'_{n+1} = \kappa'_n$ and the parameters P'^{cyc}_{ijkl} should be such that state of strain lies on the damage surface. Therefore, calculate the least squares residual as

$$RESIDUAL = \sum_{ref=1}^{N^e_{ref}} \left[\kappa' - \frac{1}{2} e'_{ij} \left(P'^{mon} (P'^{cyc})^I \right)_{ijkl} e'_{kl} \right]^2_{ref} \quad \ldots (33)$$

where N^e_{ref} is the total number of elastic unloading strain states in the reference paths considered.

- Stop if the convergence in the coefficients is achieved, i.e. ($RESIDUAL \leq TOL$). Otherwise make a new guess for the coefficients and continue iteration.

3. Store the values of coefficients obtained using least squares minimisation for subsequent use in macroscopic analysis with the HCDM model.

Figure 8(b) shows the resulting function for P'^{cyc}_{ijkl} that minimises the least squares residuals in Equations (32) and (33).

5.0 STRESS UPDATE ALGORITHM FOR MACROSCOPIC ANALYSIS

The homogenisation based continuum damage mechanics model is implemented for macroscopic finite element analysis using the user material interface (UMAT) in the commercial code ABAQUS. In an incremental solution process, subscripts n and $n + 1$ correspond to values at the beginning and end of the n–th increment respectively. At each integration point of an element in the FE model, the stresses $(\Sigma_{ij})_{n+1}$ are obtained from known values of the strain $(e_{ij})_{n+1}$ and state variables at n using the HCDM constitutive model. The essential steps in the UMAT update algorithm for the *n–th* increment are described below.

1. At the start of each iteration algorithm for solving the damage evolution problem, assume the starting value of the PDCS rotation tensor as $(Q_{ij})^0_{n+1} = (Q_{ij})_n$ and $(W_d)^0_{n+1} = (W_d)_n$.
2. For given value of $(e_{ij})_{n+1}$, and iterative value $(W_d)^I_{n+1}$, evaluate $(P'^{mon}_{ijkl})^I_{n+1}$ using Equations (21) and (24) for monotonic loading.
3. Check for damage due to monotonic loading: For the *i–th* iteration, monotonic damage evolution takes place if:

$$\frac{1}{2}(e_{ij}')_{n+1}(P'^{mon}_{ijkl})^I_{n+1}(e_{kl}')_{n+1} - \kappa_{n'} > 0$$

In this case, evaluate the scalar multiplier λ^I_{n+1} by integrating Equation (30) using backward Euler method. The damage parameters P'^{cyc}_{ijkl} are inactive during monotonic loading and assume unit values. The corresponding derivatives vanish in Equation (30). Then, the damage state variable is updated as

$$(\kappa_{n+1}')^I = \frac{1}{2}(e_{ij}')_{n+1}(P'^{mon}_{ijkl})^I_{n+1}(e_{kl}')_{n+1}$$

Proceed to step 6 to update the secant stiffness.

4. Check for damage due to cyclic loading: Evaluate $(P'^{cyc}_{ijkl})_{n+1}$ using Equation (25) for cyclic loading. The damage parameters P'^{mon}_{ijkl} are inactive during cyclic loading and assume values from previous increment ($(P'^{mon}_{ijkl})_{n+1} = (P'^{mon}_{ijkl})_n$). The corresponding derivatives vanish in Equation (30). The fatigue damage evolution takes place if: $\frac{1}{2}(e_{ij}')_{n+1}\left((P'^{mon}P'^{cyc})_{ijkl}\right)_{n+1}(e_{kl}')_{n+1} - \kappa_{n'} > 0$

In this case, evaluate the scalar multiplier λ^I_{n+1} by integrating Equation (30) using backward Euler method. The damage state variable is updated as

$$(\kappa_{n+1}')^I = \frac{1}{2}(e_{ij}')_{n+1}\left((P'^{mon}P'^{cyc})_{ijkl}\right)^I_{n+1}(e_{kl}')_{n+1}$$

Proceed to step 6 to update the secant stiffness.

5. Unloading: The applied load increment results in neutral loading or unloading if: $F' \leq 0$. In this case, proceed to step 8 with unchanged secant stiffness tensor $(E_{ijkl})_{n+1} = (E_{ijkl})_{n+1}$.

6. Determine the secant stiffness as follows:

$$(E_{ijkl}')^I_{n+1} = (E_{ijkl}')_n + (\lambda^I_{n+1} - \lambda_n)\left((P'^{mon}P'^{cyc})_{ijkl}\right)^I_{n+1} \quad \ldots (34)$$

7. Determine the PDCS rotation matrix $(Q_{ij})^I_{n+1}$ from the eigenvectors of $(D_{ij})^I_{n+1}$, corresponding to the updated secant stiffness $(E_{ij})^I_{n+1}$ using the procedure described in Section 2.1. Evaluate $(W_d)^I_{n+1}$ If convergence in the rotation matrix and $(W_d)_{n+1}$ is achieved, i.e.

$$If\ max\,|(Q_{ij})^I_{n+1} - (Q_{ij})^{I-1}_{n+1}| \leq TOL, \forall i,j = 1,2,3$$

$$and\ |(W_d)^I_{n+1} - (W_d)^{I-1}_{n+1}| \leq TOL$$

then proceed to step 8. Otherwise, return to step 2 and continue iteration.

8. Update macroscopic stresses with the converged value of the secant stiffness matrix $(E_{ijkl})_{n+1}$ as

$$(\Sigma_{ij})_{n+1} = (E_{ijkl})^I_{n+1}(e_{kl})_{n+1} \quad \ldots (35)$$

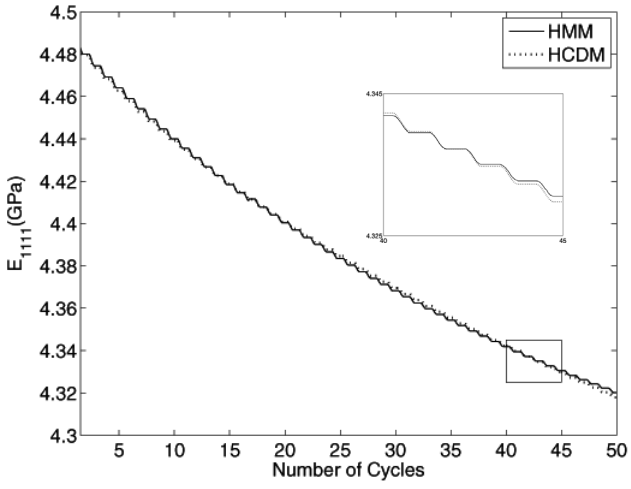
6.0 MACRO-MICRO ANALYSIS WITH THE HCDM MODEL

The orthotropic 3D homogenisation based CDM (HCDM) model is validated[1] for monotonic loading by solving numerical examples for a variety of microstructures subjected to proportional as well as non-proportional loading histories. The work presented in Ref. 1 also demonstrates the potential of HCDM model as a design tool for composite microstructures in structural applications by simulating damage progression in projectile impact. The aim of this section is to provide numerical validation and demonstrate structural applications of the 3D HCDM model for cyclic loading.

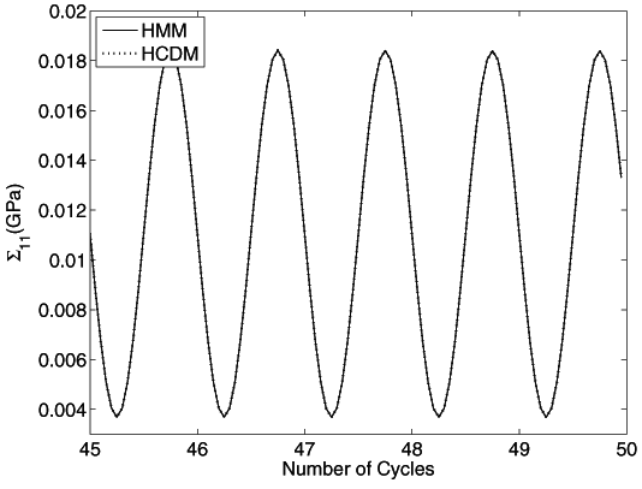
6.1 HCDM model validation for cyclic loading

The orthotropic 3D homogenisation based CDM (HCDM) model is validated for cyclic loading by solving numerical examples. Results obtained from macroscopic simulations using the HCDM model are compared with homogenised micromechanical or HMM results for the RVE. The HMM model is obtained by homogenising or volume averaging the micromechanical stresses and strains in the RVE subjected to periodic boundary conditions with imposed macroscopic strain[33]. The macroscopic finite element model implementing the HCDM constitutive relations, consists of a single eight-noded

https://doi.org/10.1017/S0001924000003043 Published online by Cambridge University Press



(a)



(b)

Figure 10. Comparison of (a) component E_{1111} of elastic stiffness tensor and (b) macroscopic stress E_{11} obtained using HCDM and HMM models for 3D RVE under cyclic tension-shear loading.

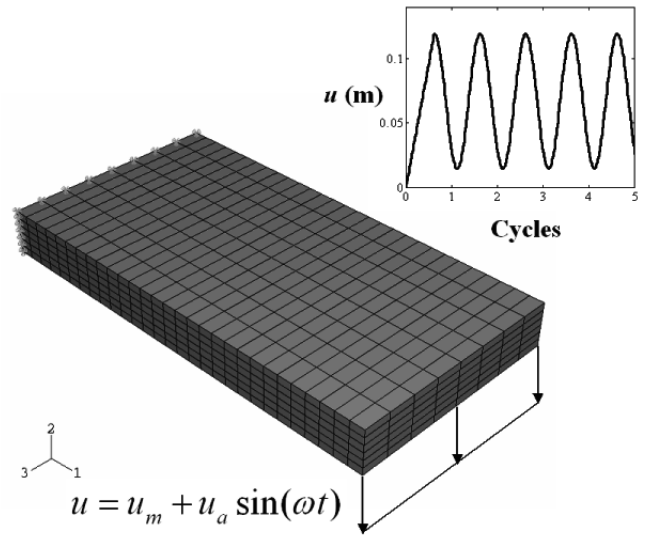


Figure 11. Finite element model of composite cantilever plate subjected to cyclic loading.

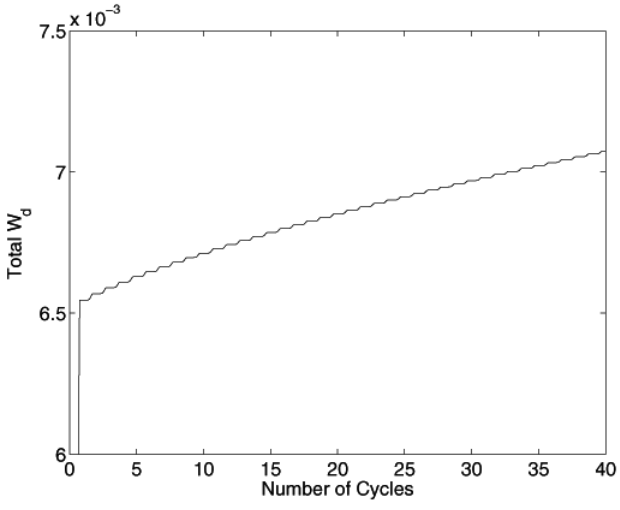


Figure 12. Total energy dissipated due to damage (W_d) in the cantilever plate due to cyclic loading.

quadrilateral element. A 3D fibre-matrix composite RVE consisting of a unit cube containing a cylindrical fibre of radius 0·2523 shown in Fig. 1(a) is considered for this validation study. Material properties of the elastic matrix are E_m = 4·6GPa, v_m = 0·4, while for the elastic fibre they are E_c = 210GPa, v_c = 0·3. The fibre volume fraction in the RVE is 20%. Cohesive zone parameters for the interface are $\delta_c = 5{\cdot}0\times10^{-5}$m, $\delta_e = 20\times10^{-4}$m, $\delta_f = 20\times10^{-3}$m and σ_m = 0·02GPa. Micromechanical analyses of the RVE are conducted by enforcing periodic displacement boundary conditions and imposing the macroscopic strain fields on the RVE.

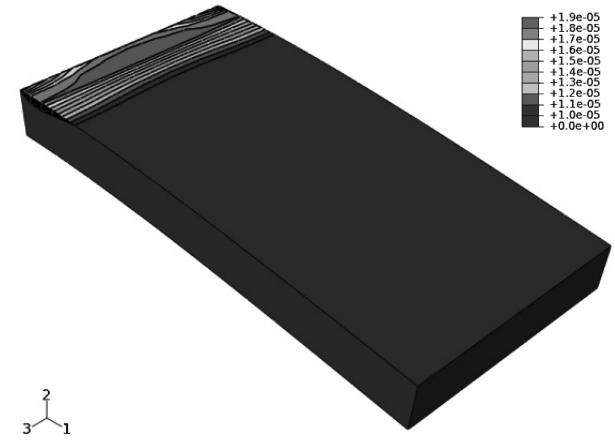
The RVE is subjected to cyclic tension-shear combined loading of $e_{ij} = \bar{e}_{ij} + \tilde{e}_{ij}\text{Sin}(2\pi t)$. Figures 10(a-b) respectively show comparison of the HCDM predictions for secant stiffness and stress with the results of HMM for 50 cycles. The excellent agreement in these plots corroborates the satisfactory performance of the HCDM model. The components of elastic stiffness tensor degrade rapidly due to monotonic damage during the first cycle (not shown), followed by steady degradation due to fatigue damage. The effectiveness of the HCDM model is evident from its CPU time of 2 mins, which is several times faster than that of HMM model with a CPU time of 175 mins.

The error in stresses predicted by the HCDM model in the above validation studies is attributed to the error in the functional representation of $\kappa'(W_d)$, P'^{mon}_{ijkl}, and P'^{cyc}_{ijkl}, as well as the assumption of orthotropy. A rigorous sensitivity study is thereby conducted to ensure accurate representation of the damage parameters such as in Equations (24) and (25). It is evident from the examples discussed that the material degradation and consequently the variation of damage parameters depends on the applied strain path. This emphasises the need for comprehensive 3D micromechanics based continuum damage model for use in macroscopic analysis modules.

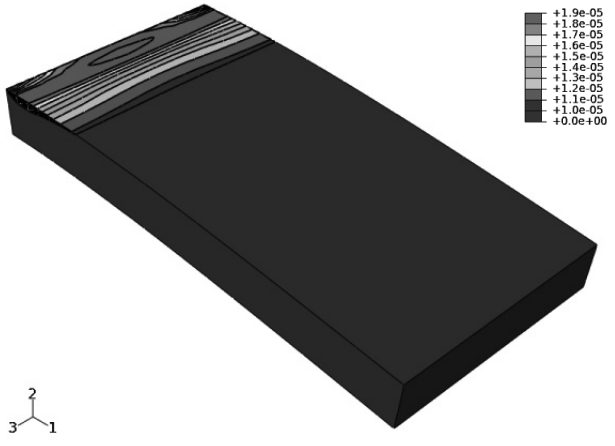
6.2 Fatigue damage in a composite cantilever

This section is intended to demonstrate the potential of HCDM model as a design tool for composite microstructures in structural applications by establishing a connection between macroscopic

https://doi.org/10.1017/S0001924000003043 Published online by Cambridge University Press



(a)



(b)

Figure 13. Contour plots of energy dissipated (W_d) due to evolving damage for composite cantilever after 40 cycles.

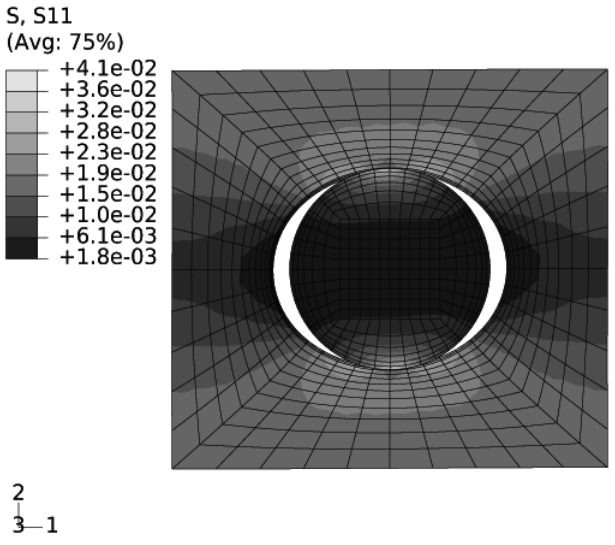


Figure 14. Contour plot of the microscopic stress (σ_{11}) in the RVE at a macroscopic point on the top surface of the cantilever near the fixed end after 40 cycles.

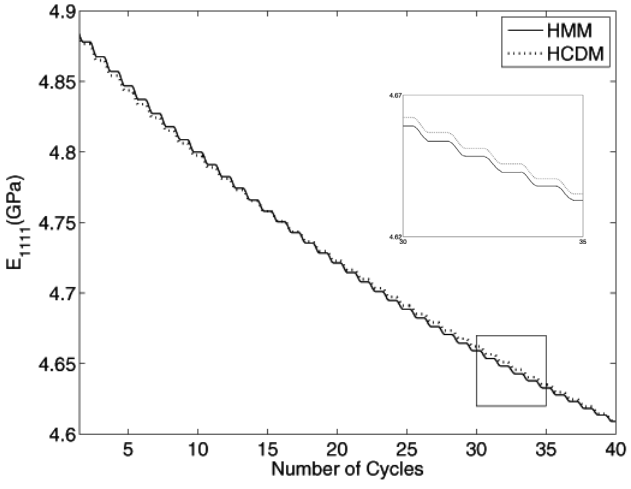


Figure 15. Comparison of component E_{1111} of elastic stiffness tensor obtained using HCDM and HMM at a macroscopic point on the composite cantilever.

damage evolution and explicit microscopic failure mechanisms. Macroscopic structural simulation of damage evolution is conducted by the commercial FEM code ABAQUS[39] with the HCDM model incorporated in the user subroutine UMAT. Once calibrated and validated, the HCDM model for a given RVE can be used for macroscopic analysis using the stress update procedure explained in Section 5. A distinct advantage of the HCDM model over conventional macro-micro homogenisation methods[40,41] is that the macroscopic analysis of large structures can be conducted very efficiently while preserving the effects of microstructural features.

A composite cantilever thick plate of 5m length, 2·5m width and 0·5m thickness is subjected to an oscillatory load at the free end as shown in Fig. 11. The cyclic behaviour of the structure is simulated using ABAQUS/Standard. The plate is constituted of microstructural RVE as described in Section 6.1. The RVE is oriented in the structure such that the local (RVE) co-ordinate system of Fig. 1(a) coincides with the global co-ordinate system of Fig. 11. The calibrated HCDM model developed in Section 4 defines the constitutive behaviour of the plate. A vertical displacement $u = \bar{u} + \tilde{u}$ Sin($2\pi t$) is applied at the free end of the cantilever plate.

The total energy dissipated due to evolving damage (W_d) in the cantilever is plotted as a function of number of cycles in Fig. 12. The total W_d increases rapidly to value of $6{\cdot}55^{-3}$ during the first cycle as the material undergoes monotonic damage. In the subsequent cycles, total W_d accumulates steadily due to fatigue damage. Figures 13(a-b) show contour plots of the dissipated energy W_d due to evolving damage after one cycle and 40 cycles respectively. During the first cycle, the structure deforms elastically until high bending stresses cause damage to initiate at the top surface near the fixed end. The damage then accumulates rapidly till the end of the first cycle with the monotonic part of the loading. After the first cycle, the degraded material points undergo steady degradation due to fatigue. This is evident from the higher values of W_d in Fig. 13(b) compared to Fig. 13(a). Subsequently, redistribution of stresses takes place resulting in accumulation of more damage in already damaged region, as well as formation of new damaged regions as seen in the contour plots.

The damage evolution in the microstructural RVE can be assessed by subjecting the RVE to the macroscopic strain history at a material point together with periodic boundary conditions. The strain history of a macroscopic point is obtained from the solution of the macroscopic problem. In the post-processor phase, the macroscopic strain history is then imposed on the RVE at any given macroscopic point

https://doi.org/10.1017/S0001924000003043 Published online by Cambridge University Press

to predict the evolution of damage. Figure 14 shows the σ_{11} contour plot in the microstructural RVE at a point on the top surface near the fixed end. The figure also shows the extent of debonding for the microstructure. The corresponding degradation of macroscopic elastic stiffness is compared in Fig. 15 with the HCDM predictions. Excellent agreement between the HCDM and the homogenised micromechanical results throughout the loading cycles confirm the robustness of the HCDM model.

7.0 CONCLUSIONS

An accurate and computationally efficient 3D homogenisation based continuum damage mechanics model (HCDM) is developed for fibre reinforced composites undergoing interfacial debonding due to cyclic loading. The HCDM model represents orthotropic behaviour of damaging composites through a fourth order damage tensor which characterises the stiffness as an internal variable. The effect of rotation of the principal damage axes due complex strain histories is accounted for by expressing the damage evolution laws in the principal damage co-ordinate system (PDCS). Functional forms of various damage parameters κ', P'^{mon}_{ijkl} and P'^{cyc}_{ijkl} are developed in terms of the invariant forms I_1, J_2 and J_3 and components of stiffness tensor E'_{ijkl} to express variation of damage variables with the evolving damage. Parameters are calibrated by performing micromechanical RVE analysis for a few imposed cyclic strain histories. The functional forms of the parameters overcome the serious limitations of constant damage parameters that are conventionally assumed in CDM models. The model's robustness is evident from the good agreement between HCDM and homogenised micromechanical (HMM) response for a variety of loading paths. The capability of the model to efficiently predict damage in structures with explicit reference to the microstructural composition is demonstrated through macro-micro analysis of a composite structure. The ability of the HCDM model to directly correlate macroscopic behaviour to the microstructural morphology, makes it a very effective tool in a material design framework to enhance the failure properties of structures.

The micromechanical model presented in this paper incorporates interfacial debonding as a representative damage mechanism. In practice, more damage modes such as matrix cracking, delamination or fibre breakage may contribute to macroscopic stiffness degradation. These can be incorporated in the micromechanics model to construct the corresponding HCDM models. The overall framework of the HCDM model will not change as a consequence. The authors are working on this aspect of multiple damage mechanisms and also on validating the HCDM model with experimental results. These will be reported in future papers.

ACKNOWLEDGEMENTS

This work has been supported by the Air Force Office of Scientific Research through grant No FA9550-06-1-0196 (Program Directors: Dr B. Les Lee and Dr V. Giurgiutiu). This sponsorship is gratefully acknowledged. Computer support by the Ohio Supercomputer Center through grant PAS813-2 is also gratefully acknowledged.

REFERENCES

1. JAIN, J.R. and GHOSH, S. Damage evolution in composites with a homogenization based contiuum damage mechanics model, *Int J Damage Mech*, 2008, (in press).
2. SURESH, S. *Fatigue of Materials*, Cambridge University Press, 1996, Cambridge.
3. HASHIN, Z. and ROTEM, A. A fatigue criterion for fiber reinforced composite materials, *J Composite Mater*, 1973, **7**, pp 448–464.
4. GATHERCOLE, N., REITER, H., ADAM, T. and HARRIS, B. Life prediction for fatigue of t800/5245 carbon-fiber composites: I. constant amplitude loading, *Int J Fatigue*, 1994, **16**, (8), pp 523–532.
5. DEGRIECK, J. and PAEPEGEM, W.V. Fatigue damage modeling of fiber-reinforced composite materials: review, *Appl Mech Rev*, 2001, **54**, (4), pp 279–300.
6. TALREJA, R. *Fatigue of Composite Materials*, 1987, Technomic Pub Co.
7. REIFSNIDER, K.L. Life prediction analysis: directions and divagations, 1987, Proceedings of Sixth International Conference on Composite Materials, **4**, pp 4.1–4.31.
8. SIDOROFF, F. and SUBAGIO, B. Fatigue damage modeling of composite materials from bending tests, 1987, Proceedings of Sixth International Conference on Composite Materials, **4**, 4.32–4.39.
9. WHITWORTH, H.A. A stiffness degradation model for composite laminates under fatigue loading, *Composite Struct*, 1998, **40**, (2), pp 95–101.
10. KACHANOV, L.M. *Introduction to Continuum Damage Mechanics*, 1987, NIJHOFF, M, Dordrecht, Boston.
11. VOYIADJIS, G.Z. and KATTAN, P.I. *Advances in Damage Mechanics: Metals and Metal Matrix Composites with an Introduction to Fabric Tensors*, 2006, Elsevier.
12. KRAJICINOVIC, D. *Damage Mechanics*, 1996, Elsevier, Amsterdam.
13. CHABOCHE, J.L. Continuum damage mechanics: A tool to describe phenomena before crack initiation, *Nuclear Enginering Design*, 1981, **64**, pp 233–247.
14. SIMO, J.C. and JU, J.W. Strain and stress-based continuum damage models, part i: Formulation, *Int J Solids Struct*, 1987, **23**, (7), pp 821–840.
15. CHOW, C.L. and WANG, J. An anisotropic theory of elasticity for continuum damage mechanics, *Int J Frac*, 1987, **20**, pp 381–390.
16. ARNOLD, S.M. and KRUCH, S. A differential cdm model for fatigue of unidirectional metal matric composites, 1991, NASA Technical Memorandum 105726.
17. BHATTACHARYA, B. and ELLINGWOOD, B. A new cdm-based approach to structural deterioration, *Int J Solids Struct*, 1999, **36**, pp 1757–1779.
18. CHOW, C.L. and WEI, Y. Constitutive modeling of material damage for fatigue failure prediction. *Int J Damage Mech*, 1999, **8**, pp 355–375.
19. DESMORAT, R., RAGUENEAU, F., and PHAM, H. Continuum damage mechanics for hysteresis and fatigue of quasi-brittle materials and structures, *Int J Numer Anal Meth Geomech*, 2007, **31**, pp 307–329.
20. FISH, J., YU, Q. and SHEK, K. Computational damage mechanics for composite materials based on mathematical homogenization, *Int J Numer Meth Engrg*, 1999, **45**, pp 1657–1679.
21. CHABOCHE, J.L., KRUCH, S. and POTTIER, T. Micromechanics versus macromechanics: a combined approach for metal matrix composite constitutive modeling, *Eur J Mech A/Solids*, 1998, **17**, pp 885–908.
22. LADEVEZE, P. An anisotropic damage theory with unilateral effects: Applications to laminates and to three- and four-dimensional composites, *Cont Damage Mech Mater Struct*, ALLIX, O. and HILD, F. (Eds), 2002, **1**, pp 205–233.
23, JU, J.W., KO, Y.F. and RUAN, H.N. Effective elastoplastic damage mechanics for fiberreinforced composites with evolutionary complete fiber debonding. *Int J Damage Mech*, 2006, **15**, (3), pp 237–265.
24. AKSHANTALA, N.V. and TALREJA, R. A micromechanics based model for predicting fatigue life of composite laminates, *Mat Sci Engrg*, 2000, **A285**, pp 303–313.
25. ECHLE, R. and VOYIADJIS, G.Z. Simulation of damage evolution in a unidirectional titanium matrix composite subjected to high cycle fatigue, *Int J Fatigue*, 1999, **21**, pp 909–923.
26. FISH, J. and YU, Q. Computational mechanics of fatigue and life predictions for composite materials and structures. *Comp Meth Appl Mech Enginering*, 2002, **191**, pp 4827–4849.
27. KRUCH, S., CARRERE, N. and CHABOCHE, J.L. Fatigue damage analysis of unidirectional metal matrix composites, *Int J Fatigue*, 2006, **28**, pp 1420–1425.
28. KOUZNETSOVA, V., BREKELMANS, W.A.M. and BAAIJENS, F.P.T. An approach to micro-macro modeling of heterogeneous materials, *Computational Mech*, 2001, **27**, pp 37–48.
29. RAGHAVAN, P. and GHOSH, S. A continuum damage mechanics model for unidirectional composites undergoing interfacial debonding, *Mech Mater*, 2005, **37**, (9), pp 955–979.
30. FEYEL, F. and CHABOCHE, J.L. Fe2 multiscale approach for modelling the elastoviscoplastic behaviour of long fibre sic/ti composite materials, *Comput Meth Appl Mech Enginering*, 2000, **183**, pp 309–330.
31. GHOSH, S., BAI, J. and RAGHAVAN, P. Concurrent multi-level model for damage evolution in microstructurally debonding composites, *Mech Mater*, 2007, **39**, (3), pp 241–266.
32. LI, S. and GHOSH, S. Debonding in composite microstructures with morphologic variations, *Int J Computational Methods*, 2004, **1**, (1), pp 21–149.

https://doi.org/10.1017/S0001924000003043 Published online by Cambridge University Press

33. JAIN, J.R. and GHOSH, S. Homogenization based 3D contiuum damage mechanics model for composites undergoing microstructural debonding, *J Appl Mech*, 2008, **75**, (3).
34. CORDEBOIS, J.P. and SIDOROFF, F. Anisotropic damage in elasticity and plasticity, *J Mech Theor Appl*, 1982, pp 45–60.
35. MURAKAMI, S. Mechanical modeling of material damage, *J Appl Mech*, 1988, **55**, pp 280–286.
36. SWAMINATHAN, S., PAGANO, N.J. and GHOSH, S. Analysis of interfacial debonding in three dimensional composite microstructures, *J Engng Mater Tech*, 2006, **128**, pp 96–106.
37. BHATNAGAR, H., WALTER, M.E., and GHOSH, S. A parametric domain map for top coat damage initiation and propagation in eb-pvd thermal barrier coatings, *Int J Multiscale Compu Engrg*, 2007, **5**, pp 227–242.
38. PELLEGRINO, C., GALVANETTO, U. and SCHREFLER, B.A. Numerical homogenization of periodic composite materials with non-linear material components, *Int J Numer Meth Engrg*, 1999, **46**, pp 1609–1637.
39. *Abaqus Users Manual*, 2001, Hibbit, Karlsson and Sorensen.
40. LENE, F. and LEGUILLON, D. Homogenized constitutive law for a partially cohesive composite material, *Int J Solids Struct*, 1982, **18**, (5), pp 443–458.
41. GUEDES, J.M. and KIKUCHI, N. Preprocessing and post processing for materials based on the homogenization method with adaptive finite element methods, *Comp Meth in Appl Mech and Engng*, 1991, **83**, pp 143–198.

APPENDIX

1. Derivatives of polynomial function $f(I_1, J_2, J_3)$ in Equations (23) and (24) with respect to strain components e'_{ij}

$$\frac{\partial f(I_1,J_2,J_3)}{\partial e_{ij}'} = \frac{\partial f}{\partial e_{kl}}\frac{\partial e_{kl}}{\partial e_{ij}'} \quad \ldots (36)$$

where, using chain rule,

$$\frac{\partial f}{\partial e_{ij}} = \frac{\partial f}{\partial I_1}\frac{\partial I_1}{\partial e_{ij}} + \frac{\partial f}{\partial J_2}\frac{\partial J_2}{\partial e_{ij}} + \frac{\partial f}{\partial J_3}\frac{\partial J_3}{\partial e_{ij}} \quad \ldots (37)$$

From expression for $f(I_1, J_2, J_3)$ in Equations (23) and (24),

$$\frac{\partial f}{\partial I_1} = a_1 + 2a_4 I_1 + a_5 J_2 + \ldots, \quad \frac{\partial f}{\partial J_2} = a_2 + a_5 I_1 + \ldots, \quad \frac{\partial f}{\partial J_3} = a_3 + \ldots \quad \ldots (38)$$

Using definitions for I_1, J_2 and J_3 in Equation (21),

$$\left[\frac{\partial I_1}{\partial e_{ij}}\right] = \frac{1}{3}\begin{bmatrix} A & 0 & 0 \\ 0 & B & 0 \\ 0 & 0 & C \end{bmatrix} \quad \ldots (39)$$

$$\frac{\partial J_2}{\partial e_{ij}} = \frac{\partial J_2}{\partial e_{kl}^d}\frac{\partial e_{kl}^d}{\partial e_{ij}} = \frac{\partial J_2}{\partial e_{kl}^d}\left(\delta_{ik}\delta_{jl} - \frac{1}{3}\delta_{kl}\delta_{ij}\right) \quad \ldots (40)$$

$$\left[\frac{\partial J_2}{\partial e_{kl}^d}\right] = 2\begin{bmatrix} H(e_{11}^d - e_{22}^d) - G(e_{33}^d - e_{11}^d) & Le_{12}^d & Me_{13}^d \\ Le_{12}^d & F(e_{22}^d - e_{33}^d) - H(e_{11}^d - e_{22}^d) & Ne_{23}^d \\ Me_{13}^d & Ne_{23}^d & G(e_{33}^d - e_{11}^d) - F(e_{22}^d - e_{33}^d) \end{bmatrix} \quad \ldots (41)$$

$$\frac{\partial J_3}{\partial e_{ij}} = \frac{\partial J_3}{\partial e_{kl}^d}\frac{\partial e_{kl}^d}{\partial e_{ij}} = \frac{\partial J_3}{\partial e_{kl}^d}\left(\delta_{ik}\delta_{jl} - \frac{1}{3}\delta_{kl}\delta_{ij}\right) \quad \ldots (42)$$

$$\left[\frac{\partial J_3}{\partial e_{kl}^d}\right] = \begin{bmatrix} O(e_{22}^d e_{33}^d) + P(e_{23}^d)^2 & 2Q(e_{12}^d e_{33}^d) + R(e_{13}^d e_{23}^d) & 2S(e_{13}^d e_{22}^d) + R(e_{12}^d e_{23}^d) \\ 2Q(e_{12}^d e_{33}^d) + R(e_{13}^d e_{23}^d) & O(e_{11}^d e_{33}^d) + S(e_{13}^d)^2 & 2P(e_{11}^d e_{23}^d) + R(e_{12}^d e_{13}^d) \\ 2S(e_{13}^d e_{22}^d) + R(e_{12}^d e_{23}^d) & 2P(e_{11}^d e_{23}^d) + R(e_{12}^d e_{13}^d) & O(e_{11}^d e_{22}^d) + Q(e_{12}^d)^2 \end{bmatrix} \quad \ldots (43)$$

2. Derivatives of polynomial function $f(I_1, J_2, J_3)$ in Equations (23) and (24) with respect to energy dissipated due to damage

$$\frac{\partial f}{\partial W_d} = \frac{\partial f}{\partial I_1}\frac{\partial I_1}{\partial W_d} + \frac{\partial f}{\partial J_2}\frac{\partial J_2}{\partial W_d} + \frac{\partial f}{\partial J_3}\frac{\partial J_3}{\partial W_d} \quad \ldots (44)$$

where

$$\frac{\partial I_1}{\partial W_d} = \frac{1}{3}\left(\frac{\partial A}{\partial W_d}e_{11} + \frac{\partial B}{\partial W_d}e_{22} + \frac{\partial C}{\partial W_d}e_{33}\right) \quad \ldots (45)$$

The derivatives $\frac{\partial I_1}{\partial W_d}$ and $\frac{\partial I_1}{\partial W_d}$ can be evaluated similarly. From defin-

ition for functions A, B, C, F... in Equation (22),

$$\frac{\partial A}{\partial W_d} = a_1^A + 2a_2^A W_d, \quad \frac{\partial B}{\partial W_d} = a_1^B + 2a_2^B W_d, \quad \frac{\partial C}{\partial W_d} \quad \ldots (46)$$

3. Derivatives of function for κ' in Equation (23)

$$\frac{\partial \kappa'}{\partial e_{ij}'} = \frac{\partial f}{\partial e_{kl}}\frac{\partial e_{kl}}{\partial e_{ij}'}\exp(f) \quad \ldots (47)$$

$$\frac{\partial \kappa'}{\partial W_{d'}} = \frac{\partial f}{\partial W_d}\exp(f) \quad \ldots (48)$$

4. Derivatives of function for P'^{cyc}_{ijkl} in Equation (25)

$$\frac{\partial P'^{cyc}_{ijkl}}{\partial e_{pq}'} = \frac{\partial P'^{cyc}_{ijkl}}{\partial \| e' \|}\frac{\partial \| e' \|}{\partial e_{pq}'} = \left(\frac{E_{ijkl}'}{d_1^{ijkl}E_{ijkl}' + d_2^{ijkl}} - \frac{2d_3^{ijkl}}{\| e' \|^3}\right)\frac{1}{\| e' \|}U_{pq} \quad \text{(nosum)} \quad \ldots (49)$$

$$\frac{\partial P'^{cyc}_{ijkl}}{\partial E_{pqrs}'} = \frac{d_2^{ijkl}\| e' \|}{\left(d_1^{ijkl}E_{ijkl}' + d_2^{ijkl}\right)^2}\delta_{ip}\delta_{jq}\delta_{kr}\delta_{ls} \quad \text{(nosum)} \quad \ldots (50)$$

https://doi.org/10.1017/S0001924000003043 Published online by Cambridge University Press